J. Fluid Mech. (1988), *vol.* 188, *pp.* 337–361
Printed in Great Britain

Developing fluid flow in a curved duct of square cross-section and its fully developed dual solutions

By W. Y. SOH

Sverdrup Technology Inc., NASA Lewis Research Center, 21000 Brookpark Road, Cleveland, OH 44135, USA

(Received 28 December 1986)

Developing fluid flow in a curved duct of square cross-section is studied numerically by a factored ADI finite-difference method on a staggered grid. A central-difference scheme with primitive variables is used inside the computational domain to reduce numerical diffusion. Two Reynolds numbers, 574 and 790, based upon a bulk velocity and hydraulic diameter are chosen for curvature ratios of 1/6.45 and 1/2.3, respectively. It is found that the secondary flow is far more complicated than expected, with the appearance of at least two pairs of vortices. Main-flow separation is also observed for the higher curvature ratio. Furthermore, it is observed that the flow develops into two quite different states downstream, depending upon the inlet conditions.

Solution of the fully developed Navier–Stokes equations is shown to be not unique beyond a certain critical Reynolds number. Developing flow seems to evolve into the fully developed state along a particular branch, into which the fully developed solution bifurcates.

1. Introduction

Fluid flow in a curved duct has played an important role in fluid mechanics because of its relevance to various engineering applications. Owing to the presence of secondary flow caused by centrifugal force, fluid flow in a curved geometry differs significantly from flow in a straight channel. Much larger pressure drop or friction, heat transfer and mixing rates are expected for a flow in a curved duct, except for very slow flow.

Since the discovery of secondary flow in a circular curved pipe by Eustice (1910, 1911) and the analytical confirmation of its existence by Dean (1927, 1928), numerous studies on the flow in curved channels with rectangular or circular cross-section have been reported for either fully developed or developing flows. For a developing flow in a curved duct Patankar, Pratap & Spalding (1974), Humphrey (1977), and Soh & Berger (1984) reported numerical calculations of flow in a circular curved pipe. Humphrey, Taylor & Whitelaw (1977) also reported flow calculations for a square curved duct. Soh & Berger (1984) showed the appearance of an additional weak vortex pair near the inner wall of a circular curved pipe in a developing region, and Humphrey, Change & Modavi (1982) reported a two-vortex-pair secondary flow downstream of a 180° turning square duct. Recently, Hille, Vehrenkamp & Schulz-DuBois (1985) found experimentally an additional weak vortex pair near the outer wall in the developing region of the 180° turning square bend. They claim that one vortex-pair of the secondary flow evolves smoothly into two vortex pairs downstream, beyond a certain critical Dean number.

Dennis & Ng (1982) and Nandakumar & Masliyah (1982) reported non-unique solutions in their calculations of fully developed flow through a circular curved pipe. They show that the solutions bifurcate into two branches if the Dean number exceeds some critical value. Along one of the branches one vortex pair, and along the other two vortex pairs, appear in the secondary flow. To obtain two vortex pairs in the circular curved pipe as an additional solution, which is bifurcated from the one-vortex-pair solution, Nandakumar & Masliyah (1982) made an elaborate effort to keep the two vortex pairs obtained from the calculation of the semicircular curved pipe flow (Masliyah 1980). They changed the cross-section geometry gradually from a semicircle to a full circle starting with the initial data from the two-vortex-pair solution. In the bifurcation phenomenon of flow in a circular curved pipe the two-vortex-pair solution is difficult to obtain unless much care is taken. This indicates that the one-vortex-pair solution is predominant over that for two vortex pairs; or it may be said that the former appears to be a more natural flow phenomenon. Nandakumar & Masliyah (1982) report that the two-vortex-pair solution is relatively easier to obtain for a curved pipe of semicircular cross-section than for a full circle. From this it may be conjectured that for flow in a curved duct of other than circular cross-section, such as a square cross-section for example, the two-vortex-pair solution is predominant over the one-vortex-pair solution beyond a certain value of the Dean number. As mentioned earlier, the experiment of Hille *et al.* (1985) shows the spatial evolution of one pair into two pairs of vortices as flow proceeds downstream. It is necessary to solve the Navier–Stokes equations numerically for developing and fully developed flows to show how the secondary flow develops as fluid travels downstream, and also to find when the additional vortex pair appears as the Dean or Reynolds number increases in the fully developed flow.

In this paper, the Navier–Stokes equations are solved numerically to elucidate the flow phenomena mentioned above. It is assumed that the flow is laminar, steady, and symmetric about the midplane of the cross-section. A central-difference scheme is employed inside the computational domain throughout the calculations lest details in the secondary flow be washed out numerically. The present central-difference scheme on a staggered grid yields stable solutions without a need for artificial damping terms. We address three primary issues. We first show how flow develops into two quite different flow patterns far downstream depending upon the inlet condition. Next, we present and discuss the dual solutions of the fully developed Navier–Stokes equations in conjunction with the downstream evolution of developing flows of different inlet conditions. And finally we describe the very complicated flow development for a highly curved duct. A topological rule is used to characterize the extremely complex secondary flow.

2. Formulation of the problem

2.1. *Governing equations*

The incompressible Navier–Stokes equations are written in dimensionless form as

$$\frac{\partial \boldsymbol{u}}{\partial t}+\nabla\cdot(\boldsymbol{u}\boldsymbol{u}) = -\nabla p+Re^{-1}\nabla^2\boldsymbol{u} = 0, \tag{1}$$

$$\nabla\cdot\boldsymbol{u} = 0, \tag{2a}$$

where $\boldsymbol{u}$, p, and Re are the dimensionless velocity, pressure, and Reynolds number, respectively. In order to obtain a steady-state solution, (1) and (2a) are to be integrated in time until the solution converges. For imcompressible flow it is not straightforward to integrate (1) and (2*a*) owing to the special role of the pressure. The continuity equation (2*a*) is not of a time-evolution form. This prohibits direct time advancement for the incompressible-flow computation, which is, however, possible in compressible-flow calculations through the equation of state. To overcome this difficulty, an artificial compressibility method introduced by Chorin (1967) is adopted. With this method, the divergence-free constraint on the velocity (2*a*) is changed into the time-evolution equation,

$$\beta \frac{\partial p}{\partial t} + \nabla \cdot \boldsymbol{u} = 0, \tag{2b}$$

where β is the coefficient of artificial compressibility always having a positive value. Equations (1) and (2*b*) can now be treated like compressible-flow equations, and can be integrated with time in a straightforward manner until a steady solution is obtained asymptotically.

The Navier–Stokes equations with artificial compressibility are written in cylindrical coordinates as

$$\frac{\mathscr{D}u}{\mathscr{D}t} - \frac{w^2}{r} = -\frac{\partial p}{\partial r} + Re^{-1}\left(\nabla^2 u - \frac{2}{r^2}\frac{\partial w}{\partial \phi} - \frac{u}{r^2}\right), \tag{3}$$

$$\frac{\mathscr{D}v}{\mathscr{D}t} = -\frac{\partial p}{\partial z} + Re^{-1}\nabla^2 v, \tag{4}$$

$$\frac{\mathscr{D}w}{\mathscr{D}t} + \frac{uw}{r} = -\frac{1}{r}\frac{\partial p}{\partial \phi} + Re^{-1}\left(\nabla^2 w + \frac{2}{r^2}\frac{\partial u}{\partial \phi} - \frac{w}{r^2}\right), \tag{5}$$

$$\beta \frac{\partial p}{\partial t} + \frac{1}{r}\left[\frac{\partial}{\partial r}(ru) + \frac{\partial}{\partial z}(rv) + \frac{\partial w}{\partial \phi}\right] = 0, \tag{6}$$

where (u, v, w) are the dimensionless velocities corresponding to (r, z, ϕ). Figure 1 shows this, with bars denoting the dimensional variables. The length, time, velocity, and pressure are made dimensionless with a, a/W_{m}, W_{m} and ρW_{m}^2, respectively. The Reynolds number Re is defined as aW_{m}/ν, where a is the side dimension of the square duct, W_{m} the bulk velocity, ρ the density, and ν the kinematic viscosity. The operators $\mathscr{D}/\mathscr{D}t$ and ∇^2 are defined as

$$\frac{\mathscr{D}\cdot}{\mathscr{D}t} = \frac{\partial \cdot}{\partial t} + \frac{1}{r}\left[\frac{\partial}{\partial r}(ru\,\cdot) + \frac{\partial}{\partial z}(rv\,\cdot) + \frac{\partial}{\partial \phi}(w\,\cdot)\right],$$

$$\nabla^2 \cdot = \frac{1}{r}\left[\frac{\partial}{\partial r}\left(r\frac{\partial \cdot}{\partial r}\right) + \frac{\partial}{\partial z}\left(r\frac{\partial \cdot}{\partial z}\right) + \frac{\partial}{\partial \phi}\left(\frac{1}{r}\frac{\partial \cdot}{\partial \phi}\right)\right].$$

Coordinate stretching is based upon the physical consideration that rapid change in the flow variables is expected to occur near the wall and the inlet regions, with

$$\left.\begin{aligned} r &= \frac{R}{a} + x(\xi) && (-0.5 \leqslant x(\xi) \leqslant 0.5) \\ z &= z(\eta) && (0 \leqslant z(\eta) \leqslant 0.5) \\ \phi &= \phi(\zeta) && (0 \leqslant \phi(\zeta) \leqslant \phi_{\mathrm{e}}) \end{aligned}\right\} \tag{7a}$$

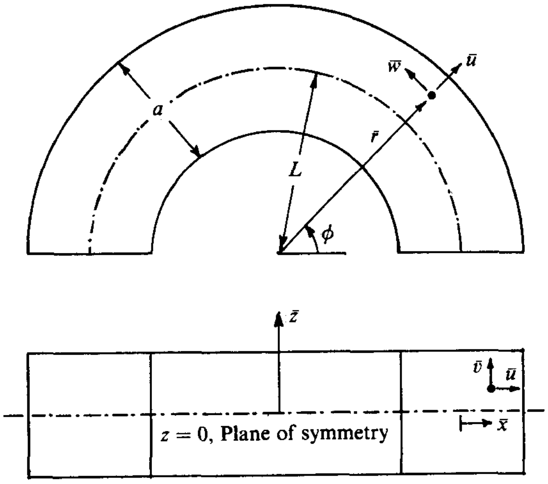

FIGURE 1. Cylindrical coordinate system.

where $x(\xi) = 0.5\tan^{-1}(s_1(\xi/I-0.5))/\tan^{-1}(0.5s_1)$, $z(\eta) = 0.5\tan^{-1}(s_2\eta/J)/\tan^{-1}s_2$, and $\phi(\zeta) = \phi_e \sinh(s_3\zeta/K)/\sinh s_3$. Here I, J, K are grid spacing numbers and s_1, s_2, s_3 are the parameters controlling grid clustering in the r-, z- and ϕ-directions. Then, the operators, $\mathscr{D}/\mathscr{D}t$ and ∇^2 become

$$\left.\begin{aligned} \frac{\mathscr{D}\cdot}{\mathscr{D}t} &= \frac{\partial\cdot}{\partial t} + \frac{1}{g}\left[\frac{\partial}{\partial\xi}(Bz'\phi'u\cdot) + \frac{\partial}{\partial\eta}(Br'\phi'v\cdot) + \frac{\partial}{\partial\zeta}(\delta r'z'w\cdot)\right], \\ \nabla^2\cdot &= \frac{1}{g}\left[\frac{\partial}{\partial\xi}\left(\frac{Bz'\phi'}{r'}\frac{\partial\cdot}{\partial\xi}\right) + \frac{\partial}{\partial\eta}\left(\frac{Br'\phi'}{z'}\frac{\partial\cdot}{\partial\eta}\right) + \frac{\partial}{\partial\zeta}\left(\frac{\delta^2 r'z'}{B\phi'}\frac{\partial\cdot}{\partial\zeta}\right)\right], \end{aligned}\right\} \qquad (7b)$$

where $B = 1+\delta x(\xi)$, $g = Br'z'\phi'$, and δ is the curvature ratio defined as a/L. A prime denotes a derivative.

2.2. *Numerical formulation*

The Navier–Stokes equations (3)–(6) can be rearranged in the (ξ, η, ζ)-coordinates for factorization in conjunction with the present numerical scheme as

$$\frac{\partial \boldsymbol{Q}}{\partial t} + (\mathbf{A}_\xi + \mathbf{A}_\eta + \mathbf{A}_\zeta)\,\boldsymbol{Q} + \boldsymbol{C} = \mathbf{0}, \qquad (8)$$

where $\boldsymbol{Q} = (u, v, w, p)^{\mathrm{T}}$, T denoting transpose, and

$$\mathbf{A}_\xi = \begin{bmatrix} \mathrm{D} & 0 & 0 & \dfrac{1}{r'}\dfrac{\partial\cdot}{\partial\xi} \\ 0 & \mathrm{D} & 0 & 0 \\ 0 & 0 & \mathrm{D} & 0 \\ \dfrac{1}{\beta g}\dfrac{\partial(Bz'\phi'\cdot)}{\partial\xi} & 0 & 0 & 0 \end{bmatrix}, \qquad \mathbf{A}_\eta = \begin{bmatrix} \mathrm{E} & 0 & 0 & 0 \\ 0 & \mathrm{E} & 0 & \dfrac{1}{z'}\dfrac{\partial\cdot}{\partial\eta} \\ 0 & 0 & \mathrm{E} & 0 \\ 0 & \dfrac{1}{\beta g}\dfrac{\partial(Br'\phi'\cdot)}{\partial\eta} & 0 & 0 \end{bmatrix},$$

$$\mathbf{A}_\zeta = \begin{bmatrix} \mathrm{F} & 0 & 0 & 0 \\ 0 & \mathrm{F} & 0 & 0 \\ 0 & 0 & \mathrm{F} & \dfrac{\delta}{B\phi'}\dfrac{\partial\cdot}{\partial\zeta} \\ 0 & 0 & \dfrac{1}{\beta g}\dfrac{\partial(\delta r'z'\cdot)}{\partial\zeta} & 0 \end{bmatrix}, \qquad \boldsymbol{C} = \begin{bmatrix} -\dfrac{\delta w^2}{B} - \dfrac{1}{Re}\left(-\dfrac{2\delta^2}{B^2\phi'}\dfrac{\partial w}{\partial\zeta} - \dfrac{\delta^2}{B^2}u\right) \\ 0 \\ \dfrac{\delta uw}{B} - \dfrac{1}{Re}\left(\dfrac{2\delta^2}{B^2\phi'}\dfrac{\partial u}{\partial\zeta} - \dfrac{\delta^2}{B^2}w\right) \\ 0 \end{bmatrix},$$

$$\mathrm{D} = \frac{1}{g}\frac{\partial}{\partial\xi}\left[(Bz'\phi'u\cdot) - \left(\frac{Bz'\phi'}{r'}\frac{\partial\cdot}{\partial\xi}\right)\right], \quad \mathrm{E} = \frac{1}{g}\frac{\partial}{\partial\eta}\left[(Br'\phi'v\cdot) - \left(\frac{Br'\phi'}{z'}\frac{\partial\cdot}{\partial\eta}\right)\right],$$

$$\mathrm{F} = \frac{1}{g}\frac{\partial}{\partial\zeta}\left[(\delta r'z'w\cdot) - \left(\frac{\delta^2 r'z'}{B\phi'}\frac{\partial\cdot}{\partial\zeta}\right)\right]$$

Equation (8) is of the same weak-conservative form as (3)–(6). To advance (8) with time from time step n, which is the present time where the solution is known, to the time step $n+1$, we approximate the convective velocities u, v, w in the D, E, F with the values at the time step n, which are denoted by u^n, v^n, w^n. Also $\boldsymbol{C}$ is kept constant at the value at the time step n. Introducing intermediate time steps denoted by superscripts * and ** we can integrate (8) as

$$\frac{(\boldsymbol{Q}^* - \boldsymbol{Q}^n)}{\Delta t} + \mathbf{A}_\xi \boldsymbol{Q}^* + (\mathbf{A}_\eta + \mathbf{A}_\zeta)\boldsymbol{Q}^n + \boldsymbol{C}^n = 0,$$

$$\frac{(\boldsymbol{Q}^{**} - \boldsymbol{Q}^n)}{\Delta t} + \mathbf{A}_\xi \boldsymbol{Q}^* + \mathbf{A}_\eta \boldsymbol{Q}^{**} + \mathbf{A}_\zeta \boldsymbol{Q}^n + \boldsymbol{C}^n = 0,$$

$$\frac{(\boldsymbol{Q}^{n+1} - \boldsymbol{Q}^n)}{\Delta t} + \mathbf{A}_\xi \boldsymbol{Q}^* + \mathbf{A}_\eta \boldsymbol{Q}^{**} + \mathbf{A}_\zeta \boldsymbol{Q}^{n+1} + \boldsymbol{C}^n = 0.$$

Briley & McDonald (1980) introduced a compact form of the above, which is called the 'delta form', as

$$(\mathbf{I} + \Delta t\,\mathbf{A}_\xi)\,\Delta\boldsymbol{Q}^* = -\Delta t(\mathbf{A}_\xi + \mathbf{A}_\eta + \mathbf{A}_\zeta)\,\boldsymbol{Q}^n - \Delta t\,\boldsymbol{C}^n \tag{9}$$

$$(\mathbf{I} + \Delta t\,\mathbf{A}_\eta)\,\Delta\boldsymbol{Q}^{**} = \Delta\boldsymbol{Q}^* \tag{10}$$

$$(\mathbf{I} + \Delta t\,\mathbf{A}_\zeta)\,\Delta\boldsymbol{Q}^{n+1} = \Delta\boldsymbol{Q}^{**} \tag{11}$$

where $\Delta\boldsymbol{Q}^* = \boldsymbol{Q}^* - \boldsymbol{Q}^n$, $\Delta\boldsymbol{Q}^{**} = \boldsymbol{Q}^{**} - \boldsymbol{Q}^n$, $\Delta\boldsymbol{Q}^{n+1} = \boldsymbol{Q}^{n+1} - \boldsymbol{Q}^n$, and $\mathbf{I}$ is the identity matrix. If we call (9), (10) and (11) the ξ-, η- and ζ-sweep, respectively, the u-velocity is coupled with the pressure p during the ξ-sweep. Similarly, v and w are coupled with p for each η- and ζ-sweep, respectively, in the staggered grid. The present factored ADI scheme on the staggered grid is a direct extension of a two-dimensional calculation by Soh (1987).

2.3. *Boundary conditions*

The flow field under consideration is an 'in-and-out flow' surrounded by a rigid wall. A no-slip condition is given at the wall. At the inlet and exit planes, which are drawn arbitrarily in the flow field to define a computational domain, all the velocity components except the pressure are specified at the inlet. At the exit, however, only the pressure is specified. These boundary conditions are imposed under the assumption that there is no streamwise flow reversal through these planes. At the wall

$$u = v = w = 0 \quad \text{at } x = \pm 0.5, \quad z = 0.5. \tag{12}$$

Owing to the presence of a plane of symmetry, computation is performed in only a half-domain of the cross-section with the symmetry boundary condition

$$\frac{\partial u}{\partial z} = \frac{\partial w}{\partial z} = v = 0 \quad \text{at } z = 0. \tag{13}$$

At the inlet we assume the secondary-flow velocity components, u and v, to be

$$u = v = 0 \quad \text{at } \zeta = -0.5. \tag{14}$$

The boundary condition (14) is imposed at a half-grid distance ahead of $\phi = 0$ because of the staggered grid. Figure 2 shows the in-and-out flow boundary condition in the ζ-direction. In this study the increments in the spatial variables ($\Delta\xi$, $\Delta\eta$, $\Delta\zeta$) are set to unity. For axial velocity at the inlet two different conditions on w are imposed: (i) a fully developed flow profile in a straight duct of square cross-section; (ii) a free-vortex distribution. The latter condition is chosen from the physical consideration that uniform flow entering a curved pipe (e.g. flow into a bend immediately after a reservoir) develops quickly into a free-vortex profile (Agrawal, Talbot & Gong 1978). For condition (i) an exact solution for w is given as

$$w = m\left[\sum_{l=0}^{\infty} \alpha_l \cos\lambda_l x \cosh\lambda_l z + \tfrac{1}{2}x^2 - \tfrac{1}{8}\right] \quad \text{at } \phi = 0 \quad (\text{i.e. } \zeta = 0), \tag{15a}$$

where

$$\alpha_l = \frac{4(-1)^l}{\lambda_l^3 \cosh(0.5\lambda_l)}, \quad \lambda_l = (2l+1)\pi,$$

and

$$m = 0.25\left[\sum_{l=0}^{\infty} \frac{(-1)^l \alpha_l}{\lambda_l^2} \sinh(0.5\lambda_l) - \tfrac{1}{48}\right]^{-1}.$$

The value of m represents the product of Reynolds number and the dimensionless pressure gradient, $m = Re\,(\partial p/\partial s)$, where s is a downstream variable in a straight duct. For boundary condition (ii)

$$w = \frac{w_0}{1 + \delta x(\xi)} \quad \text{at } \phi = 0 \quad (\text{i.e. } \zeta = 0), \tag{15b}$$

where w_0 is chosen such that the integration of w over the entire lower and upper halves of the cross-section becomes unity (i.e. $\iint w \, \mathrm{d}x \, \mathrm{d}z$ = flow rate = 1).

For the calculation of the w-momentum equation, which is the ζ-component of (8), at the end cell (i.e. at $k = K$; k is the grid index in the ζ-direction) only the pressure is given at the exit, allowing pressure variation over the exit cross-section about a fixed pressure level. The pressure distribution can be obtained by dropping the $\partial/\partial t$ terms in $\mathscr{D}/\mathscr{D}t$ and then integrating the ξ- and η-component of (8):

$$\left.\begin{aligned} p(i,1,K+1) &= p(1,1,K+1) + \int r'\left\{-\frac{\mathscr{D}u}{\mathscr{D}t} + \frac{\delta w^2}{B}\right. \\ &\qquad \left. - \frac{1}{Re}\left[\nabla^2 u - \frac{2\delta^2}{B^2\phi'}\frac{\partial w}{\partial \zeta} - \frac{\delta^2 u}{B^2}\right]\right\}\mathrm{d}\xi, \\ p(i,j,K+1) &= p(i,1,K+1) + \int z'\left[-\frac{\mathscr{D}v}{\mathscr{D}t} + \frac{1}{Re}\nabla^2 v\right]\mathrm{d}\eta, \end{aligned}\right\} \tag{16}$$

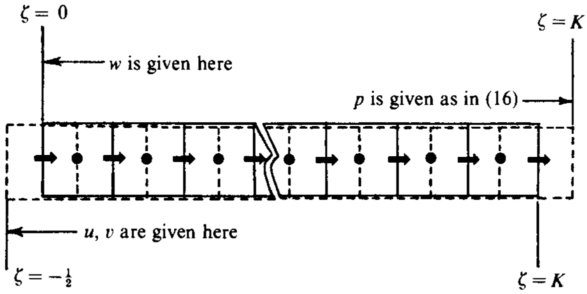

FIGURE 2. Staggered grid in the ζ-direction and in-and-out flow boundary conditions. ●, p; →, w; ——, p-cell; - - - -, w-cell.

were i and j are grid indices in the r- and z-directions, respectively. The previously mentioned fixed pressure level is with reference to setting $p(1, 1, K+1)$ constant, which is set to zero in the current calculations. Elliptic effects of the Navier–Stokes equations would adjust the upstream pressure in accordance with the downstream pressure boundary condition (16), yielding pressure gradients which have physical meaning in a steady incompressible flow. For real compressible flow we have no freedom to choose the fixed pressure level arbitrarily because the value of pressure itself has physical meaning. The integrands of (16) are calculated through extrapolation using adjacent internal points. The details of the finite-difference formulation in the staggered grid and the imposed boundary conditions can be found in Soh (1987).

2.4. *Fully developed flow formulation*

The Navier–Stokes equations for fully-developed flow can be written by eliminating derivatives with respect to the downstream variable under the assumption that the pressure gradient in the downstream direction is constant. Unlike the developing-flow case, the bulk velocity W_m, or Reynolds number, for the fully developed case is not known *a priori* but is a part of the solution. Because of this the velocity should be non-dimensionalized by some reference velocity. Soh & Berger (1987) give the reference velocity as

$$W_r = \left[\frac{a}{\rho L}\left(-\frac{\partial \bar{p}}{\partial \phi}\right)\right]^{\frac{1}{2}} = \left(\frac{aG}{\rho}\right)^{\frac{1}{2}}, \tag{17}$$

where $\bar{p}$ is the dimensional static pressure and G the pressure gradient. Non-dimensionalizing the length, velocity, pressure and time by a, W_r, ρW_r^2, and a/W_r, respectively, reduces (3)–(6) to

$$\left.\begin{aligned}
\frac{\mathscr{D}\tilde{u}}{\mathscr{D}t} - \frac{\tilde{w}^2}{r} &= -\frac{\partial \tilde{p}}{\partial r} + \frac{1}{Re_0}\left(\nabla^2 \tilde{u} - \frac{\tilde{u}}{r^2}\right),\\
\frac{\mathscr{D}\tilde{v}}{\mathscr{D}t} &= -\frac{\partial \tilde{p}}{\partial z} + \frac{1}{Re_0}\nabla^2 \tilde{v},\\
\frac{\mathscr{D}\tilde{w}}{\mathscr{D}t} + \frac{\tilde{u}\tilde{w}}{r} &= \frac{1}{B} + \frac{1}{Re_0}\left(\nabla^2 \tilde{w} - \frac{\tilde{w}}{r^2}\right),\\
\beta\frac{\partial \tilde{p}}{\partial t} + \frac{1}{r}\left[\frac{\partial}{\partial r}(r\tilde{u}) + \frac{\partial}{\partial z}(r\tilde{v})\right] &= 0,
\end{aligned}\right\} \tag{18}$$

where the tilde denoted dimensionless quantities based upon W_r. Re_0 is the reference

Reynolds number defined as aW_r/ν. The term B^{-1} appearing in the $\tilde{w}$-momentum equation is the constant pressure gradient maintaining the flow. The operators, $\mathscr{D}/\mathscr{D}t$ and ∇^2, are as given in (7*b*) without derivatives with respect to ϕ. The coordinate transformation in the r- and z-directions is also the same as in (7*a*).

Because W_r, or consequently Re_0, is merely a parameter, for a physical interpretation it is necessary to find a relation between W_r and W_m, or between Re_0 and Re. This can be done by considering the flow rate through half of the cross-section, with

$$\left.\begin{aligned} &0.5W_m = bW_r,\\ \text{where}\quad &b = \int_0^{\frac{1}{2}}\int_{-\frac{1}{2}}^{\frac{1}{2}} \tilde{w}\,\mathrm{d}x\,\mathrm{d}z,\\ \text{therefore}\quad &Re/Re_0 = 2b. \end{aligned}\right\} \tag{19}$$

3. Results and discussion

3.1. *Definition of the Dean number*

After Dean (1927) various definition of a dimensionless number, which is now called the Dean number, have been introduced depending upon their use. Definition of the Dean number for developing flow differs from that for fully developed flow. To avoid possible confusion only one Dean number, $\kappa = Re\,\delta^{\frac{1}{2}}$, is introduced here. This has been used both by those who conduct experiments and by those who analyse developing flow. κ is also a readily derivable quantity for fully developed flow, as will be shown later.

3.2. *Run conditions for numerical calculations*

For developing-flow calculations two flow conditions are selected: Case (I) $Re = 574$ with $\delta = 1/6.45$ (i.e. $\kappa = 226$); and Case (II) $Re = 790$ with $\delta = 1/2.3$ (i.e. $\kappa = 521$). Case (I) is investigated for two different inlet conditions; (i) fully developed straight-duct flow as given in (14) and (15*a*); and (ii) a potential vortex profile as in (14) and (15*b*). We denote Case (I–i) and Case (I–ii) to be Case (I) for inlet conditions (i) and (ii), respectively. For Case (II), only the fully developed straight-duct flow condition at the inlet is considered. Concerning the grid, $(I \times J \times K)$ equal to $16 \times 11 \times 24$ and $20 \times 13 \times 28$ grid points are used for Cases (I–i, ii) and (II), respectively. The run conditions, including the artificial compressibility β, the time step Δt and the convergences, are listed in table 1. The maximum and root-mean-square of $\nabla \cdot \boldsymbol{u}$ are denoted by $\max(\nabla \cdot \boldsymbol{u})$ and r.m.s. $(\nabla \cdot \boldsymbol{u})$, respectively. $\mathrm{Max}(u)$, $\max(v)$ and $\max(w)$ are the maximum values of residuals of the r-, z- and ϕ-components of $\nabla \cdot (\boldsymbol{uu}) + \nabla p - Re^{-1}\nabla^2\boldsymbol{u}$, respectively. The exit angle, ϕ_e in (7*a*), is set to be 180° for all cases. The difference in the flow rate between the inlet and the exit when converged is less than 0.05% of the inlet flow rate for all cases. Computations have been carried out on an IBM 370/3033. The CPU times for the convergences listed in table 1 are about 1.2, 1.4, and 3.2 h for Cases (I–i), (I–ii) and (II), respectively.

3.3. *Main-flow development for Case (I)*

For the case with the fully developed straight-channel flow profile at the inlet, which is Case (I–i), the flow is symmetric about $x = 0$ and has its maximum there on the plane of symmetry (i.e. $z = 0$). Immediately after the flow enters the turning duct this symmetry in the axial velocity is broken. This is because the flow is subject to a centrifugal acceleration which causes faster moving fluid particles to travel towards the outer wall. This also leads to the appearance of the maximum velocity near the

Case	β	Δt	s_1	s_2	s_3	$\max(\nabla\cdot\boldsymbol{u})$	r.m.s. $(\nabla\cdot\boldsymbol{u})$	$\max(u)$	$\max(v)$	$\max(w)$	Number of time steps
(I–i)	0.15	0.06	3	1	1.5	3.0×10^{-6}	1.4×10^{-6}	1.2×10^{-4}	5.3×10^{-5}	3.2×10^{-4}	1690
(I–ii)	0.20	0.08	3	1	1.5	3.0×10^{-6}	8.5×10^{-7}	2.8×10^{-4}	1.4×10^{-4}	3.0×10^{-4}	1870
(II)	0.15	0.07	3	1.5	1.5	8.5×10^{-6}	1.0×10^{-6}	4.7×10^{-4}	4.1×10^{-4}	2.4×10^{-4}	2300

TABLE 1. Run conditions

outer wall. Figure 3(*a*(i)–*d*(i)) shows the development of the axial flow on the plane of symmetry for Case (I–i). In the region of early flow development the location of the maximum axial velocity on the plane of symmetry, which is denoted by x_{m}, becomes shifted towards the outer wall from its initial position $x=0$ at $\phi=0$ as shown in figure 3(*a*)(i) owing to the centrifugal effect. At $\phi=26.8°$, x_{m} reaches 0.34 and only moves a little further outward up to $\phi=44°$. At about $\phi=44°$, x_{m} arrives at its maximum value of 0.348. This agrees very well with the experiment of Hille *et al.* (1985), which shows that x_{m} reaches 0.35 near $\phi=36°$. In this early region of development the value of the maximum axial velocity $w_{\max}$ on the plane of symmetry decreases as fluid travels downstream. Also the value of w in the wide area near the centre at $x=0$ becomes smaller, which is shown by the arrow in figure 3(*a*)(i). In the downstream region after about 44°, x_{m} moves gradually inside towards the centre with $w_{\max}$ being further reduced. Unlike the flow in the early developing region, w on $z=0$ increases near the centre (see the arrow in figure 3*b*(i)). The innermost value of x_{m} is about 0.25 at 99.3° and stays there up to about 116.5° with $w_{\max}=1.66$. Farther downstream the axial flow exhibits little change with the exception of small oscillations in the velocity profile near the centre. This profile shows decreasing (figure 3*c*(i)) and then increasing (figure 3*d*(i)) values of w on $z=0$ far downstream. Figure 3(*d*)(i) shows no significant variation in w with the downstream variable ϕ. It seems that the axial flow is reasonably fully developed near the exit.

The axial-flow development for Case (I–ii) is shown in figure 3(*a*(ii)–*d*(ii)). The plateau-like flat area near the centre, which is a potential core, is gradually eroded and shifted outward as the flow proceeds downstream. From about 44° the potential core becomes no longer discernible. Figure 3(*a*)(ii) illustrates this early stage of the flow development. After about 44° the axial velocity profiles on $z=0$ are similar in shape to those of Case (I–i) downstream, as shown in figure 3(*b*)(ii). In this region, x_{m} shifts continuously outward until it reaches a value of 0.27 at about 83.8° with $w_{\max}=1.64$. After this maximum shift towards the outer wall, x_{m} retreats slowly towards the centre with $w_{\max}$ still increasing, as shown in figure 3(*c*)(ii). The value of $w_{\max}$ is 1.67 at about 135.4°. Farther downstream the value of $w_{\max}$ becomes smaller and x_{m} migrates continuously towards the centre. Figure 3(*d*)(ii) shows the inward movement of x_{m} together with the decrease of $w_{\max}$ on $z=0$. It is noted that the axial velocity is still changing even at the exit, which indicates that for Case (I–ii) the axial flow is far from being fully developed. The axial velocity profile for the fully developed flow in figure 3(*d*)(ii) is obtained by solving the fully developed-flow equation (18) using $Re_0=180$, which gives $Re=586$.

For Case (I–i) the pressure at the inner bend (i.e. $x=-0.5$, $z=0$) decreases smoothly all the way to the exit. On the other hand, it is found that there is a

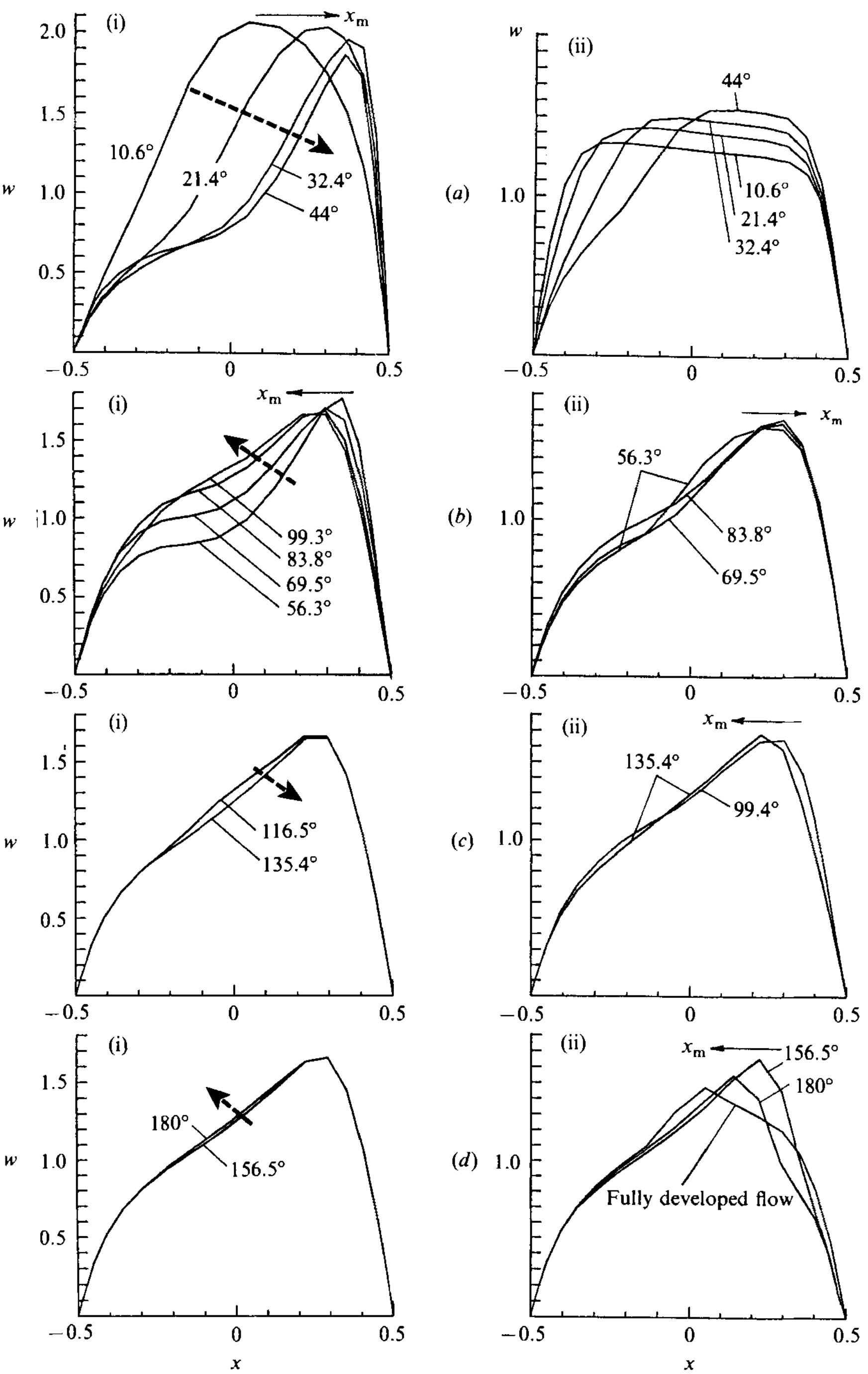

FIGURE 3. Axial velocity profile on the plane of symmetry: (*a*(i), *b*(i), *c*(i), *d*(i)) for Case (I–i); (*a*(ii), *b*(ii), *c*(ii), *d*(ii)) for Case (I–ii).

pressure rise yielding an adverse pressure gradient along the outer bend (i.e. $x = 0.5$, $z = 0$) in the region close to the inlet. Calculation does not indicate a streamwise flow separation at the outer wall despite the adverse pressure gradient. This may be because the adverse pressure gradient is weak, and it exists only for a short distance downstream for this particular value of Re and δ. For Case (I–ii) the pressure drops abruptly on both the inner and outer bends because of a sudden development of the axial-flow boundary layer immediately after the inlet. There is no adverse pressure gradient on both sides of the wall in the downstream direction.

3.4. *Secondary-flow development for Case (I)*

Because of the assumption that the flow is symmetric about $z = 0$, the secondary flow will be discussed only in the upper half of the cross-section. As the flow enters the curved duct a secondary flow develops immediately. The secondary flow for Case (I–i) already exhibits a large-vortex structure at the first grid in the ϕ-direction, which is $\phi = 2.6°$ for the calculation of u and v. As shown in figure 4 the secondary flow sets up in a such a way that fluid flows counterclockwise along solid walls toward the inner bend while it is being pushed outward through the core region near the plane of symmetry. The secondary flow becomes rapidly intensified up to about 24°. For $\phi \lesssim 18.6°$ the secondary flow near the plane of symmetry is outward, and is of the same order of magnitude as that near the upper wall. At about 18.6° the maximum value of the secondary-flow speed $(u^2+v^2)^{\frac{1}{2}}$ is about 0.34 on $z = 0$ and about 0.36 near the upper wall. This intensified secondary flow directed outward near $z = 0$ and the centrifugal force $\delta w^2/(1+x)$ efficiently convey fast moving fluid particles towards the outer wall. This can be seen from figure 3(*a*)(i). At about 21.4°, x_{m} is already shifted up to 0.3, which is high considering that the maximum value of x_{m} is 0.348 at 44°. The secondary flow near the upper wall is further intensified up to 24°, where the maximum value of $(u^2+v^2)^{\frac{1}{2}}$ is about 0.46 at about $x = 0.1$ and $z = 0.45$. For $\phi \gtrsim 24°$ it becomes weaker, especially in the area of the plane of symmetry and the corners. From approximately the downstream position where the secondary flow weakens, the vortex centre moves towards the inside. Figure 4 at about 41° shows this with the appearance of a severely distorted primary vortex.

Downstream at about 53.2°, the secondary flow exhibits increasing complexity with the appearance of crossflow reversal near the inner bend, two large corotating vortices, and multiple points where a change in flow direction occurs on the plane of symmetry. The secondary-flow velocity on $z = 0$, which is u, becomes extremely small at 53.2°, and remains small for $\phi \lesssim 80°$. At about 66°, an additional weak vortex appears at the outer wall, and the secondary flow is directed inward on the entire plane of symmetry. This observation agrees very well with the experiment of Hille *et al.* (1985), which shows that the second vortex starts at about 60°. Their two-vortex-pair structure in the entire cross-section (see their figure 10) is essentially very close to the present result at 95.3° in figure 4, where the primary vortex and additional weak vortex are observed. At about 80° the vortex near the inner bend due to the crossflow reversal vanishes and the large corotating vortices begin to merge into a single primary vortex, which is shown at 80.1° and 95.3° in figure 4. However, after the large corotating vortices merge, the weak vortex near the outer bend vanishes at about 125° forming a single primary-vortex structure, and then appears again farther downstream of $\phi \gtrsim 156°$.

An additional calculation using $\phi_{\mathrm{e}} = 240°$ also indicates that the weak vortex near the outer bend disappears at about 128°, which is very close to 125° obtained using $\phi_{\mathrm{e}} = 180°$. However, this weak vortex reappears farther downstream. This forms the

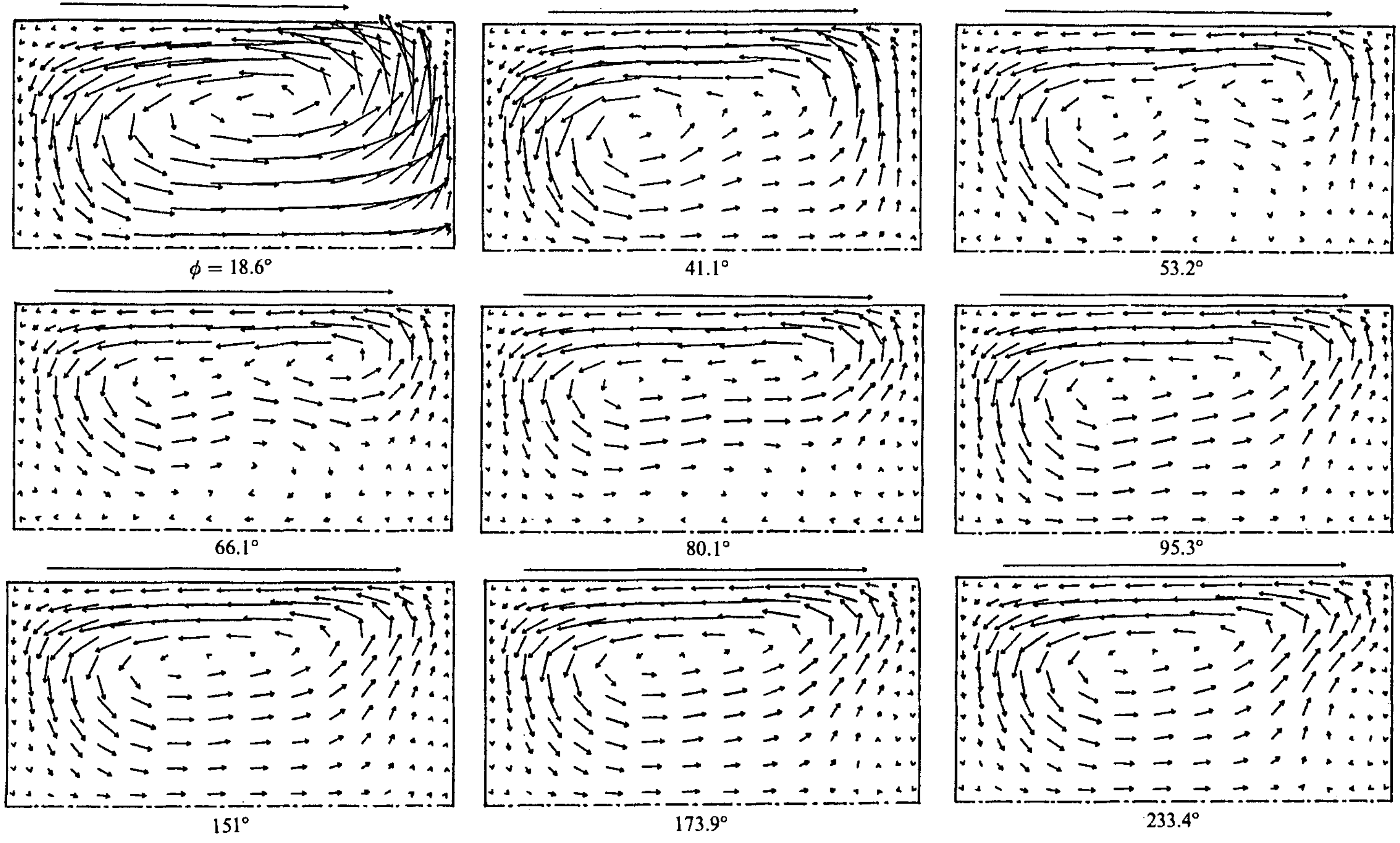

FIGURE 4. Secondary-flow development for Case (I–i).

two-vortex structure downstream of $\phi \gtrsim 160°$; one is the primary vortex, and the other is the weak vortex near the outer wall. The two-vortex structure persists downstream to the exit, which is $\phi = 240°$ in the additional calculation.

For Case (I–ii) the secondary flow experiences a quite different flow development from Case (I–i). At the very beginning immediately after the inlet, streamlines of the secondary flow depart from the wall towards the centre. The centre behaves like a sink-type node as shown at 2.6° in figure 5. As the node shifts outward, $x = 0.3$ at 7.9°, a large primary vortex begins to form and the secondary flow is intensified with its vortex centre shifted towards the inside. In Case (I–ii) the secondary flow is less complicated than that in Case (I–i); neither secondary-flow reversal near the inner wall nor dividing of the primary vortex into two occurs. The single vortex persists up to about 80°, and then evolves into the two-vortex structure in the secondary flow. As shown at 95.3°, an additional vortex forms near the outer bend and is then intensified. As shown at 151° and 173.9°, the vortex located near the outer wall is no longer minor but of the same strength as the primary vortex. The further development of the axial flow and the secondary flow downstream into a truly fully developed state is readily seen in the trend of the axial-flow development downstream in figure 3(*d*)(ii), and by comparing the downstream secondary-flow vector plot in figure 5 with figure 6(*d*). As shown previously in figure 3(*d*)(ii), the appearance of $w_{\max}$ near the centre for the fully developed axial velocity profile is easy to understand, because fast moving fluid particles are being pushed inward owing to the presence of the additional strong vortex at the outer bend despite the effect of centrifugal force. This fully developed axial flow profile in figure 3(*d*)(ii) has almost the same shape as those given by Dennis & Ng (1982) and Nandakumar & Masliyah (1982) as the additional solution, which has the two-vortex-pair solution in the entire cross-section.

3.5. *Fully developed flow*

As mentioned earlier, the downstream evolution of developing flow depends upon the inlet condition. For Case (I–i) the maximum value of the axial velocity $w_{\max}$ appears greatly shifted towards the outer bend, and one primary vortex with a weak vortex near the outer wall develops at the exit. For Case (I–ii) the location of the maximum velocity on the plane of symmetry moves towards the centre, and two equally strong vortices are observed at the exit. With these totally different downstream evolutions of developing flows, the nature of the ultimate flow at a hypothetically large distance downstream arises as an immediate question. To answer this it is necessary to solve the fully developed Navier–Stokes equations (18). Solutions of (18) are obtained for $\delta = 1/6.45$ by choosing the time step Δt and β to be 0.15–0.4 and 0.1–0.2, respectively.

The friction ratio f_c/f_s is defined as the ratio of the pressure gradient in a curved duct to that in a straight one for the same flow rate. That is,

$$\frac{f_c}{f_s} = \left(\frac{1}{L}\frac{\partial \bar{p}}{\partial \phi}\right)\bigg/\left(\frac{\partial \bar{p}}{\partial \bar{s}}\right),$$

where $\bar{s}$ is the dimensional downstream variable in the straight duct. Using (17), (15*a*) and (19) gives the friction ratio as

$$\frac{f_c}{f_s} = \frac{(\rho/a)\,W_r^2}{(\rho W_m^2/a)\,(\partial p/\partial s)} = \left(\frac{W_r}{W_m}\right)^2 \frac{Re}{m} = \frac{Re_0^2}{m\,Re}. \tag{20}$$

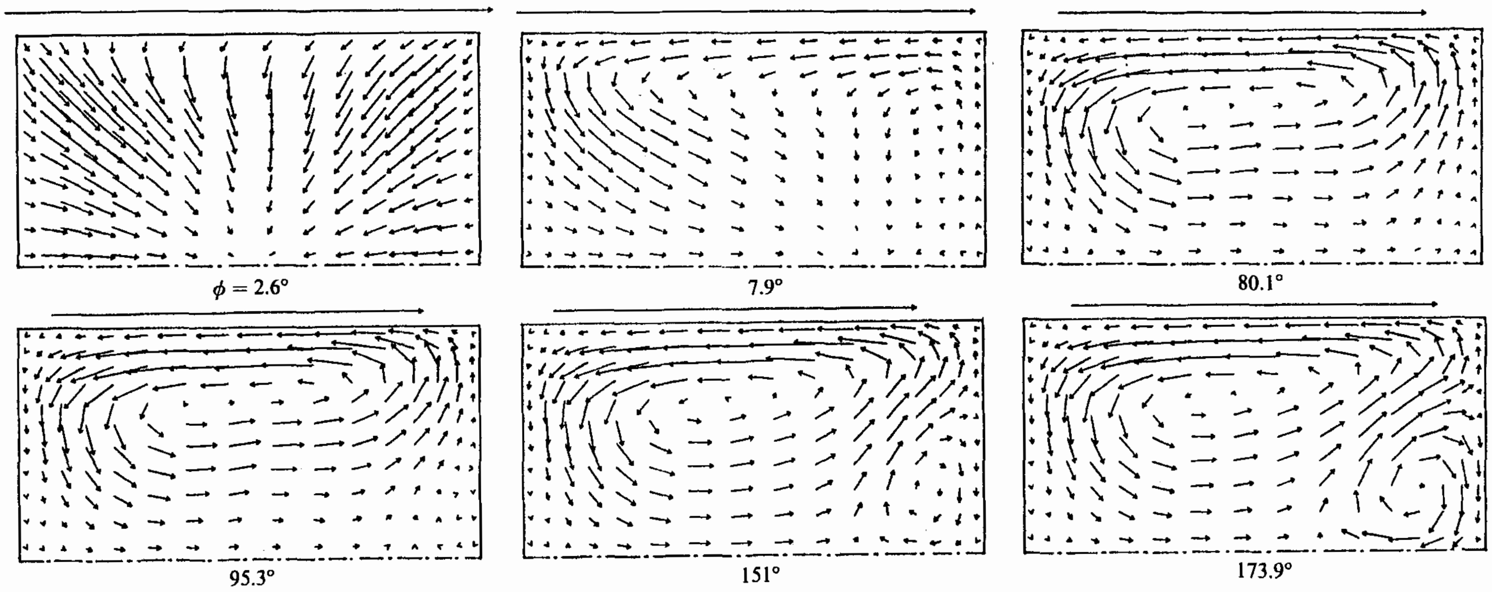

$\phi = 2.6°$ 7.9° 80.1°

95.3° 151° 173.9°

FIGURE 5. Secondary-flow development for Case (I–ii).

The value of m for a duct of square cross-section is 28.4542. The Dean number κ is defined by (19) as

$$\kappa = Re\,\delta^{\frac{1}{2}} = 2b\,Re_0\,\delta^{\frac{1}{2}}. \tag{21}$$

In the numerical investigation a solution was obtained first for $Re_0 = 60$, and solutions for higher Re_0 were sought successively by increasing Re_0 with each previous solution as initial data. From $Re_0 = 110$, whose solution is of a single vortex, Re_0 was increased by 10. This gives two large vortices in the secondary flow for $Re_0 = 120$. The two-vortex solutions for $Re_0 > 120$ are easily obtained by increasing Re_0. Another attempt was made in such a way that Re_0 was increased by small increments from $Re_0 = 110$. A series of solutions for $Re_0 = 112$, 113, 115, 116, and 117 was obtained by increasing Re_0 gradually, which are still of one vortex. At $Re_0 = 118$, an additional weak vortex begins to form near the outer wall, and it grows as Re_0 increases up to 120. But it should be noted that the weak vortex near the outer bend remains minor compared with the primary vortex as shown in figure 6 (b(i), c(i)). At $Re_0 = 120$, Re_0 was increased by 0.5 for the next solution at $Re_0 = 120.5$, and two large vortices appear. The present calculation fails to predict the solution of one primary vortex with the weak vortex at the outer wall beyond $Re_0 = 120$. A bifurcation point has been obtained by decreasing the value of Re_0. The critical Dean number κ_1 where the bifurcation occurs is about 116.5 for $\delta = 1/6.45$.

Figure 7 shows the friction ratio f_c/f_s against $\kappa^{\frac{1}{2}}$. It can be seen that f_c/f_s is proportional to $\kappa^{\frac{1}{2}}$ for the wide range of Dean number used here, except for the Dean-number region immediately after κ_1 along the upper curve. Values of W_r/W_m $(= 2b)$, Re, κ, and f_c/f_s for given Re_0 are presented in table 2. For $113 < Re_0 < 120$ the numbers appearing first denote the values along the lower branch. For $\kappa < 116.5$ only one solution is obtained for each Re_0, or corresponding κ. From about $\kappa = 116.5$ the f_c/f_s curve becomes bifurcated into two branches, which will be called upper and lower branches. Along the upper branch a sudden appearance of two large vortices is observed even at $Re_0 = 113$ (i.e. $\kappa = 116.57$ and see figure 6a(ii)), an increase of only 1 from $Re_0 = 112$ where a single vortex is obtained. One vortex is observed along the lower branch at the same $Re_0 = 113$ (i.e. $\kappa = 118.17$ for the lower branch). This is shown in figure 6(a)(i). Along the upper branch, two large vortices are well maintained for increasing Re or κ.

A smooth transition from a one- to a two-vortex solution is observed along the lower branch. Up to $Re_0 = 117$ (i.e. $\kappa = 124.99$) only one vortex appears, but as Re_0 increases the additional vortex begins to form at about $Re_0 = 118$ (i.e. $\kappa = 126.71$). When this additional vortex appears convergence is very slow in the numerical calculation. This newly formed vortex grows as Re_0 increases until it reaches 120 (i.e. $\kappa = 130.20$ along the lower branch), but it still remains weak. Beyond $Re_0 = 120$, at 120.5 for example, the solution disappears from the lower branch and jumps into the upper branch. No solution is found for $Re_0 > 120$ along the lower branch under the symmetry assumption about $z = 0$. The weak vortex near the outer bend is of the Taylor–Görtler type: a counter-rotating vortex pair caused by centrifugal instability occurring in a boundary layer along a concave wall. It is interesting to compare the lower and upper branches with the downstream flow fields of Case (I–i) and Case (I–ii), respectively. Downstream flow for Case (I–ii) is of the same type as the flow observed along the upper branch, in which two equally strong vortices are obtained and x_m is located near the centre. It should be noted that although the flow for Case (I–ii) is not yet fully developed at $\phi = 180°$, the trend of development is towards the flow solution of the upper branch. This can be readily realized by comparing the secondary-flow vector plot at the exit in figure 5 with that

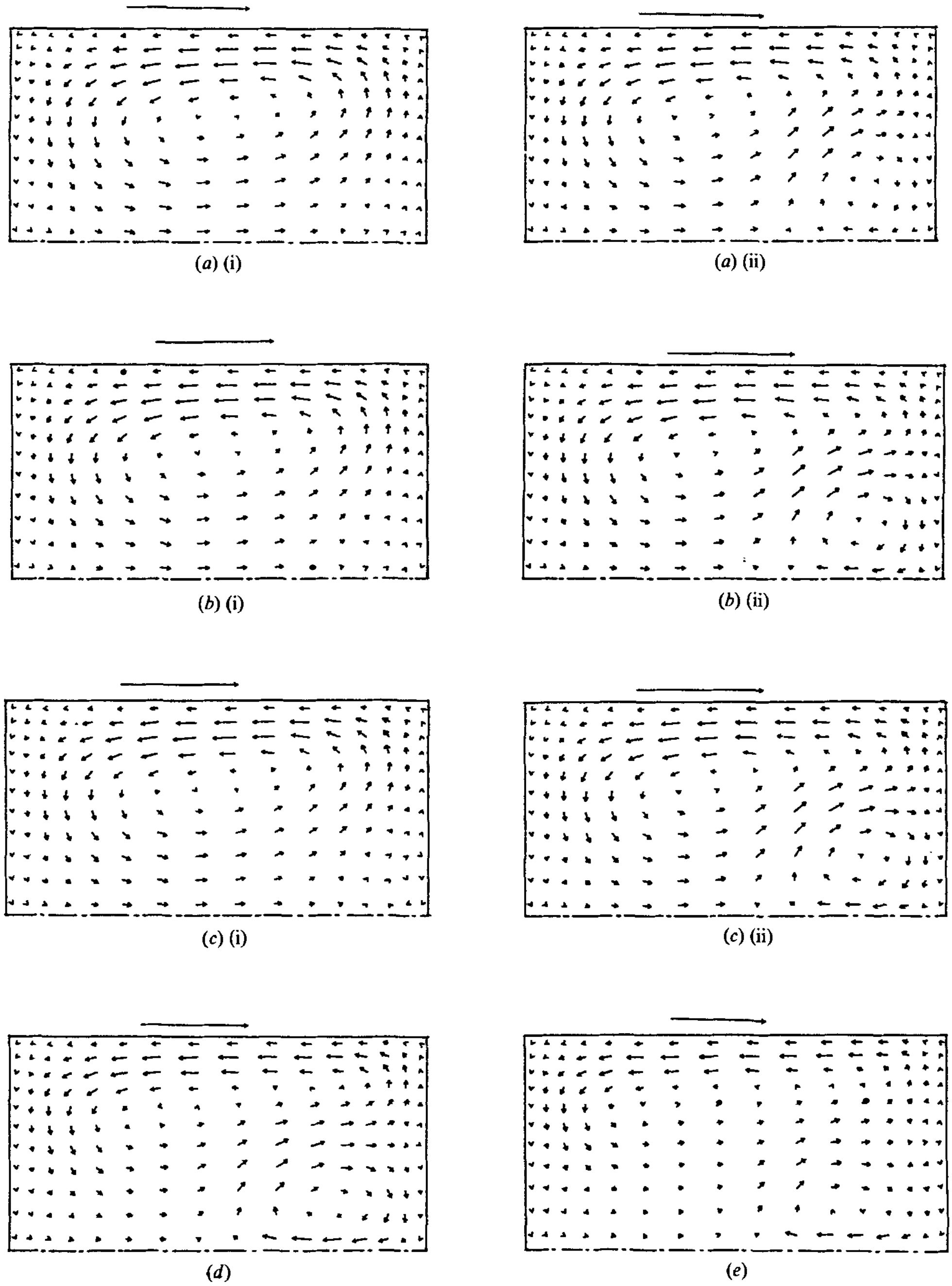

FIGURE 6. Fully developed secondary flow for $\delta = 1/6.45$. (*a*)(i), (ii) $Re_0 = 113$; (*b*)(i), (ii), 118; (*c*)(i), (ii), 120; (*d*) 180; (*e*) 230. (*a*(i), *b*(i), *c*(i)) and (*a*(ii), *b*(ii), *c*(ii), *d*, *e*) are the secondary-flow plots along the lower and the upper branches, respectively.

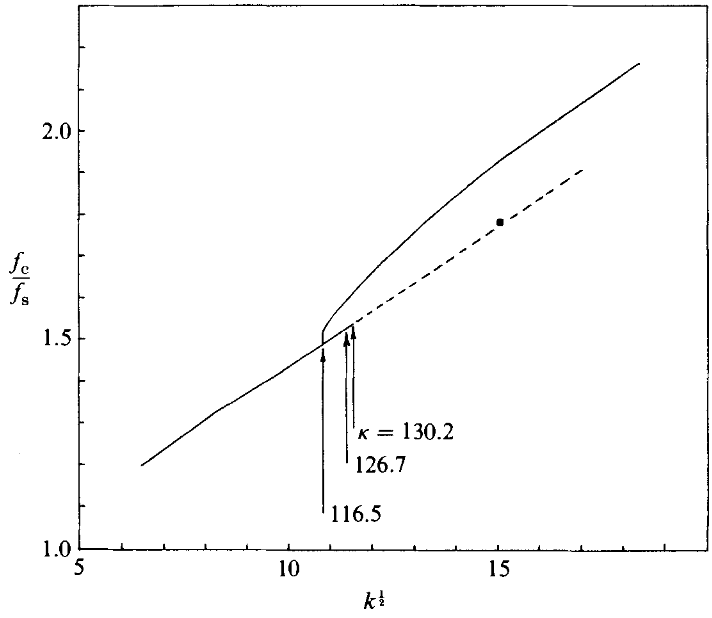

FIGURE 7. Variation of the friction ratio with $\kappa^{\frac{1}{2}}$.

Re_0	W_r/W_m	Re	κ	f_c/f_s
60	0.5683	105.58	41.57	1.198
80	0.4705	170.04	66.95	1.323
100	0.4065	245.99	96.86	1.429
110	0.3828	287.34	113.14	1.480
112	0.3786	295.84	116.49	1.490
113	0.3765/0.3817	300.12/296.04	118.17/116.57	1.495/1.516
115	0.3725/0.3802	308.73/302.49	121.56/119.11	1.505/1.537
117	0.3686/0.3778	317.43/309.67	124.99/121.93	1.516/1.554
118	0.3667/0.3766	321.81/313.36	126.71/123.39	1.521/1.562
119	0.3648/0.3753	326.21/317.10	128.45/124.86	1.526/1.569
120	0.3629/0.3740	330.66/320.87	130.20/126.34	1.531/1.577
120.5	0.3733	322.78	127.09	1.581
121	0.3727	324.69	127.84	1.585
123	0.3700	332.39	130.88	1.600
126	0.3661	344.15	135.51	1.621
130	0.3610	360.12	141.80	1.649
140	0.3488	401.43	158.06	1.716
150	0.3374	444.62	175.07	1.778
160	0.3267	489.74	192.83	1.837
170	0.3167	536.86	211.39	1.892
180	0.3072	586.03	230.75	1.943
200	0.2897	690.32	271.81	2.036
210	0.2818	745.19	293.42	2.080
220	0.2745	801.45	315.57	2.122
230	0.2679	858.40	337.99	2.166

TABLE 2. Reynolds and Dean numbers, and friction ratio at $\delta = 1/6.45$

at $Re_0 = 180$ in figure 6d, and by observing the inward movement of x_m downstream in figure 3(d)(ii).

Since the solution along the lower branch cannot be obtained for $Re_0 > 120$, the plot of f_c/f_s against $\kappa^{\frac{1}{2}}$ is simply extrapolated by a straight line for $Re_0 > 120$ (i.e. $\kappa > 130.2$ along the lower branch). The pressure gradient $\partial p/\partial\phi$ for Case (I–i) is calculated to be 0.572 (0.578 in the additional calculation) at the exit, whose corresponding friction ratio f_c/f_s is 1.79. This value of the friction ratio marked with a black dot in figure 7 closely follows a straight line which is extended from $Re_0 = 120$ by a dashed line. Therefore, it can be said that the downstream flow solution of Case (I–i) is of the type of the lower branch, and that Hille *et al.*'s finding of the downstream flow pattern with the additional vortex is also of the lower-branch type, in which the smooth transition from one to two vortex pairs occurs in the entire cross-section.

Then, the question arises as to why the lower-branch type of the fully developed solution is extremely difficult or impossible to obtain for $Re_0 > 120$. It should be noted that the lower-branch solution is being sought under the symmetry assumption about $z = 0$ even for sufficiently large Re_0. Benjamin (1978) has reported the three-cell mode of a Taylor vortex between concentric cylinders with a finite length. Cliffe & Mullin (1985) also found the appearance of odd number of vortices beyond a certain Reynolds number in the Taylor-experiment problem. The fluid flow between cylinders is no longer symmetric about the midplane between stationary endwalls in the presence of the odd number of vortices. Recently, Winters (1984) reported an asymmetric solution for the fully developed fluid flow in a curved tube of rectangular cross-section. With those symmetry-breaking flow patterns it may be considered that the symmetric flow of lower-branch type is not possible beyond a certain Re_0. The appearance of an asymmetric flow structure reported by Hille *et al.* (see the symmetry-breaking secondary flow pattern in their figure 10) may also support this, although their secondary-flow structure is essentially the same as predicted by the present developing-flow calculation under the symmetry assumption about $z = 0$ in the sense that the secondary flow has the primary vortex with the additional weak vortex at the outer wall. It can be also imagined that the flow with inlet velocity given by (15a) evolves to be asymmetric far downstream. This suggests the possible existence of a fully developed solution in a different form. The fully developed-flow equations, which have been thought of as the Navier–Stokes equations with no derivatives with respect to the downstream variable, assuming a constant pressure gradient in the downstream direction, may no longer be valid for the purpose of seeking the lower-branch solution beyond a certain Reynolds number (i.e. $Re_0 > 120$ and $\delta = 1/6.45$ in this study). Another form of the fully developed solution, which is of the lower-branch type for large Reynolds or Dean number, may exist in such a way that the flow changes periodically in the downstream direction.

Winters (1984) showed two limiting points and the symmetry-breaking bifurcation point (L_1, L_2, and B in his notation) in the plot of the mean axial velocity against the pressure gradient. The first limiting point L_1 is $Dn = 80.1$ (i.e. $\kappa = 113.3$, where Dn is the Dean number he has used), the second limiting point L_2 is $Dn = 89.1$ (i.e. $\kappa = 126$), and the point B is $Dn = 91.7$ (i.e. $\kappa = 129.7$). Comparing these points with our critical values of Dean number indicated in figure 7, we can interpret the limiting point L_1 as the bifurcation point $\kappa_1 = 116.5$, L_2 as the transition point from the one to two vortices occurring at $\kappa_2 = 126.7$ along the lower branch, and B as the maximum Dean number $\kappa_3 = 130.2$ beyond which no symmetric solution is obtained on the lower branch. The symmetry-breaking point appears immediately after

$\kappa_2 = 126.7$ where a smooth transition from the one to two vortices occurs. The counter-rotating vortices of Taylor–Görtler type (taking into account the lower half of the cross-section) which appear weak and small near the outer bend from $\kappa_2 = 126.7$ readily interact with each other. Once interaction occurs the additional vortices begin to move and they swing up and down in the presence of a small asymmetric perturbation. This causes the flow to be asymmetric and does not allow the flow to be fully developed far downstream.

Since the symmetry-breaking interaction between the weak vortices occurs on a small scale within a limited area bounded by the primary vortex and the outer wall, it does not seem to affect the overall flow situation (e.g. primary vortex, axial flow profile, pressure gradient, etc.). That is why the value of the friction ration calculated at the exit of developing flow agrees very well with that predicted by the extension of the straight line in figure 7.

3.6. *Flow development in a highly curved duct for Case (II)*

As Reynolds number and curvature ratio increase, the flow development displays more complicated phenomena. For $Re = 790$ and $\delta = 1/2.3$ (i.e. $\kappa = 521$) with the fully developed straight-duct velocity at the inlet, the axial-flow development in the entrance region immediately after the inlet is similar to that for Case (I–i). However, it is noted from figure 8 that the axial flow near the inner bend undergoes a rapid change in which w decreases quickly forming a step-like velocity profile at about $37° < \phi < 47°$. For $\phi > 47.5°$ the step which appears flat near the inner wall becomes severely eroded to yield a second maximum near the inner bend. The first maximum, which is $w_{\max}$ of course, is shifted toward the outer wall. At about 47.5° the first maximum value of w on $z = 0$ appears shifted to $x = 0.36$, with the second maximum at $x = -0.3$. The valley between the two maxima remains deep up to about 70° where the location of the first maximum is $x = 0.4$.

The step profile appearing near inner bend at 47.5° has been reported experimentally by Agrawal *et al.* (1978) and numerically by Soh & Berger (1984) for flow in a curved pipe of circular cross-section. The axial velocity profile with two maxima and a deep valley on the plane of symmetry is also reported experimentally by Humphrey *et al.* (1977) for a curved duct of square cross-section. Although their values of Re and δ are identical with the present ones, it is not possible to compare the current results directly with their experimental data because their experiment has been carried out for flow in a 90° turning duct attached to long straight ducts both upstream and downstream. However, there is some quantitative agreement; their values of the first maximum of w, which are about 1.9 at 60° and 1.8 at 90° agree very well with $w_{\max} = 1.91$ at 58.2°, 1.81 at 88° and 1.76 at 94.8° of the present calculations. If the axial velocity profile is drawn on the plane parallel to $z = 0$, the second maximum appears sharper and the valley runs deeper. The valley on the plane of symmetry begins to be filled for $\phi > 70°$ and becomes flat farther downstream as shown at 159.7° and 180° in figure 8. The value of $w_{\max}$ on $z = 0$ becomes smaller and is about 1.67 near the exit. However, there still remains a vestige of the valley in the axial velocity profile on the plane (e.g. $0.28 < z < 0.36$) parallel to the plane of symmetry even at 180°.

Figure 9 shows the pressure variation along the inner and outer bends on $z = 0$, which are approximately at $i = 1$ and $j = 1$, and $i = 16$ and $j = 1$, respectively. The pressure at the inner bend decreases monotonically with ϕ, whereas there is a considerable pressure rise along the outer wall causing the streamwise flow separation.

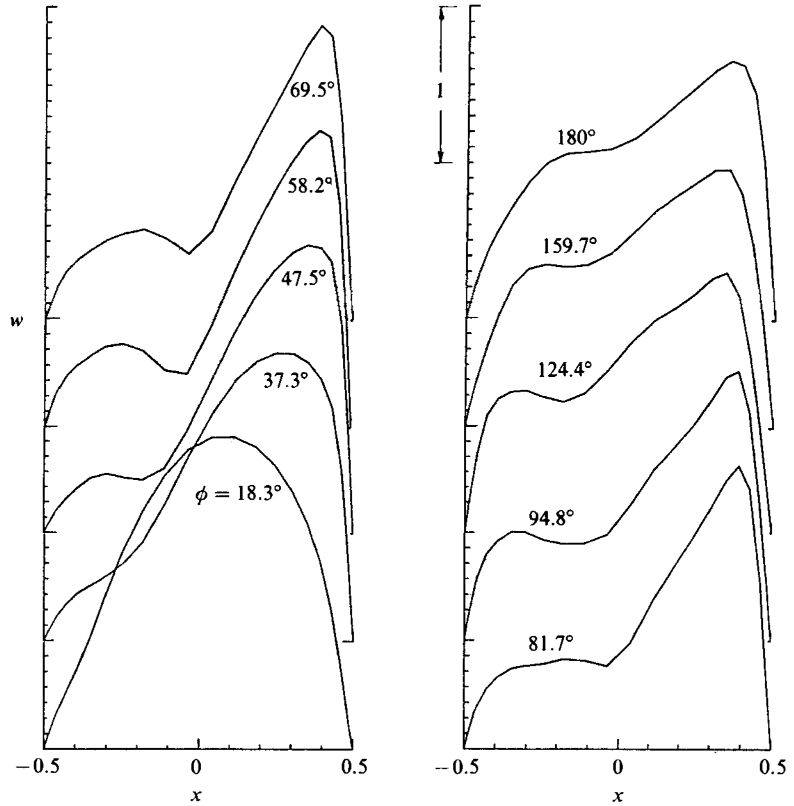

FIGURE 8. Axial-flow development on the plane of symmetry for Case (II).

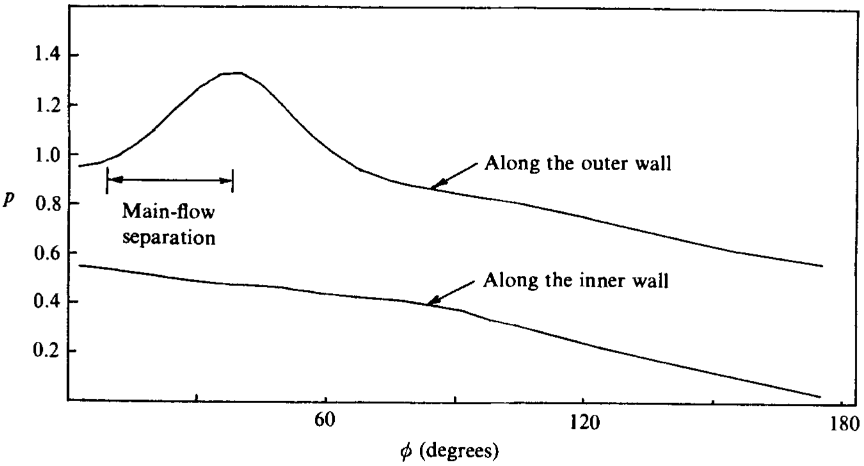

FIGURE 9. Pressure variation with ϕ along the inner and outer walls.

Early development of the secondary flow for Case (II) is similar to that for Case (I–i) in that the primary vortex forms immediately after the inlet and then becomes intensified as shown in figure 10. The magnitude of the secondary flow becomes very large. For example, the value of $(u^2+v^2)^{\frac{1}{2}}$ becomes 0.6 near the upper wall ($x = 0.15$, $z = 0.45$) at 25°, 0.83 ($x = 0$, $z = 0.45$) at 35° and reaches its maximum value of 0.87 ($x = -0.08$, $z = 0.45$) at about 40°. The secondary flow is intensified over the entire cross-section, especially near the solid wall and on the plane of symmetry. Starting from about 25° two small recirculating zones appear in the secondary flow near the upper corners of the outer and inner walls. This is shown at 34.9° in figure 10.

The streamwise-flow reversal, which is of a bubble-type separation, is observed only near the upper corner of the outer bend for about $9° \lesssim \phi \lesssim 37.4°$. It is clear from the secondary-flow development for about $\phi \lesssim 45°$ that despite the presence of the adverse pressure gradient, the axial-flow separation would not occur at the outer bend near the plane of symmetry because the secondary flow directed outside on $z = 0$ is so powerful that the axial-flow boundary layer at the outer bend on $z = 0$ becomes 'squeezed' by the oncoming secondary flow. Consequently, the linear momentum near the outer wall is large enough on $z = 0$ to overcome the adverse pressure force. The magnitude of the secondary flow is very small before and during the duration of the minor vortex near the upper corner at the outer bend. This leads to virtually no contribution of the secondary flow to the axial flow development there, and of course the axial velocity itself is small in the corner region owing to the strong viscous effect. Therefore, the axial flow with small momentum there succumbs to the adverse pressure force and separates.

At about 45° an additional secondary-flow reversal occurs at the inner bend near $z = 0$ with the primary vortex severely distorted and elongated. This crossflow reversal is deemed to be responsible for the appearance of the step-like axial velocity profile, which will be further eroded to render the second maximum with a deep valley for $\phi > 47.5°$ in figure 8. Figure 10 at 55.4° shows this extremely distorted primary vortex. Then, at 66.6° the primary vortex is divided into two large corotating vortices with vanishing of the minor vortex near the upper corner at the outer bend.

The kinematic plausibility of the complicated secondary flow under the assumption that the flow is symmetric about $z = 0$ may be demonstrated by a topological rule. Kao, Burstadt & Johns (1983) introduce a rule which is applicable to streamlines in the cross-section of a duct with no centre body (i.e. simply connected cross-section geometry), as

$$\Sigma_N + \Sigma_S + \tfrac{1}{2}(\Sigma_{N'} + \Sigma_{S'}) = 1, \tag{22}$$

where Σ_N denotes the sum of the indices for node points, Σ_S the sum of the indices for saddle points, and subscripts N' and S' denote the half-node and half-saddle on the solid boundary of the cross-section, respectively. The index value of N is 1 and S is -1.

The sketches in figure 10 illustrate the local behaviour of the secondary-flow streamlines on the upper half of the cross-section showing the node (shown as a cross) and saddle (black dot) at different downstream positions. At 66.6°, where the distorted primary vortex is divided, the secondary-flow streamlines exhibit a stagnation-type saddle between the corotating primary vortices. The nodes are of focus type. In this case, for example, taking into consideration the symmetric secondary flow in the lower half of the cross-section, the summations of each index are $\Sigma_N = 8$, $\Sigma_S = -3$ (two in the upper and lower halves of the cross-section, and one on the plane of symmetry), $\Sigma_{N'} = 0$, and $\Sigma_{S'} = -8$, so that (22) holds. It is noted from

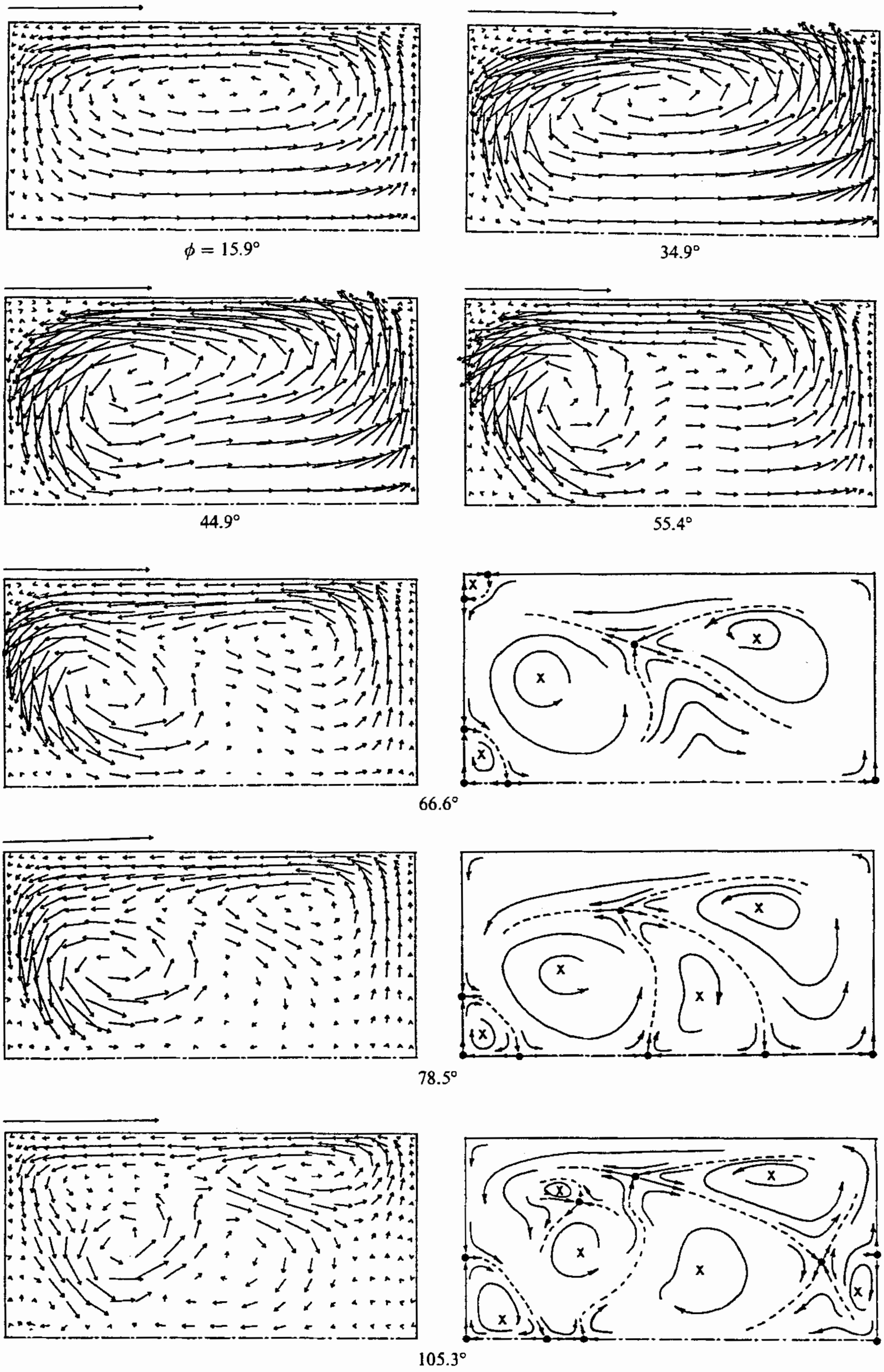
$\phi = 15.9°$

34.9°

44.9°

55.4°

66.6°

78.5°

105.3°

FIGURE 10. For caption see facing page.

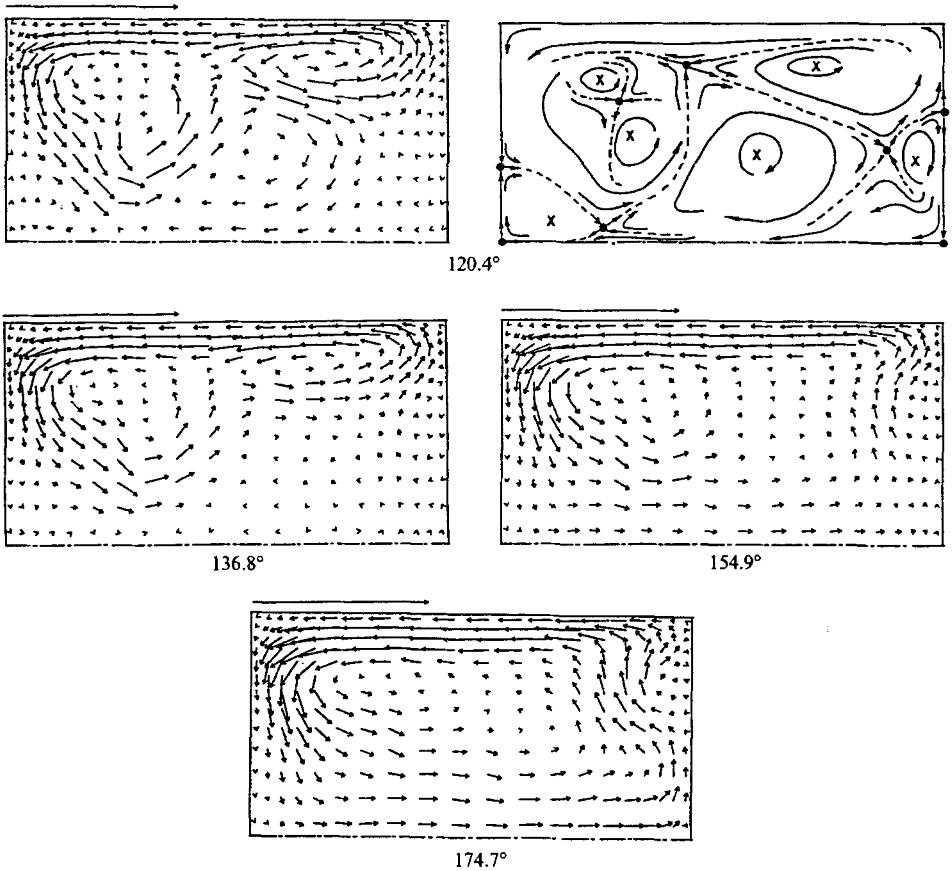

FIGURE 10. Secondary-flow development for Case (II): ×, node; ●, saddle point.

the sketch at 66.6° that the streamlines in the area neighbouring the corotating vortices are highly wavy. The wavy streamlines develop into another large vortex in such a way that they form a counter-rotating vortex structure relative to the existing two corotating vortices as shown at about 78.5°. It is also noted that the vortex due to the secondary-flow reversal near the inner bend becomes larger in size and strength as the flow develops downstream. One of the corotating vortices at the left side becomes further divided into another pair of corotating vortices (see figure 10 at 105.3°, 120.4°) with a gradually developing additional vortex at the outer bend. When this occurs it is very difficult to discern the locations of the node and the saddle owing to the limited grid resolution. However, with the help of the kinematic requirement (22) we may determine possible places for the additional node and saddle, as shown at 105.3° and 120.4° in the sketches. Figure 10 at 120.4° shows the most complicated secondary-flow structure. From a closer look at the saddles marked with black dots on $z = 0$ from 78.5° it can be seen that they move closer and merge into one, which is finally lifted from the plane of symmetry as shown at 120.4°. When this lift of the node from $z = 0$ occurs, the secondary flow is directed inside on the entire plane of symmetry even in the presence of the secondary-flow reversal at the inner bend. After this lift of the node the secondary-flow reversal at the inner bend vanishes, as shown in the vector plot at 136.8°.

At about 137° the secondary flow again exhibits two corotating primary vortices, which are merged into a single primary vortex. As shown at about 154.9° one of the corotating vortices at the right side appears to be engulfed by the other at the left side. From the last vector plot of the secondary flow in figure 10 it can be seen that the additional vortex, which is weak also, is located away from the plane of symmetry. The downstream location at 174.7° is the last position of the u, v and p calculations. Calculation shows that even at the exit the secondary flow is changing significantly, which indicates that the flow is not fully developed until much farther downstream.

4. Conclusion

Fluid flow in a curved duct of square cross-section for $Re = 574$ and $\delta = 1/6.45$ (i.e. $\kappa = 226$) develops into quite different states downstream, depending upon the inlet condition. With the appearance of dual solutions of the fully developed Navier–Stokes equations, it can be said that the flow becomes fully developed along either of two branches into which the solution is bifurcated. It is also found that there are three critical Dean numbers for $\delta = 1/6.45$. (i) $\kappa_1 = 116.5$ is the first, called the bifurcation point, below which only there is one solution of the one-vortex type, and above which two solutions are obtained. (ii) $\kappa_2 = 126.7$ is the second, above which an additional weak vortex (Taylor–Görtler type) is observed at the outer wall along the lower branch. (iii) The third is $\kappa_3 = 130.2$, above which a lower-branch solution is no longer obtained under the symmetry assumption because of the asymmetric vortex interaction in the small scale near the outer bend, and the flow presumably becomes periodic in the downstream direction.

To confirm the lower-branch-type downstream-flow behaviour it is necessary to employ much finer grids near the outer bend imposing a periodic in-and-out flow boundary condition for an appropriate interval in the downstream direction.

The author is grateful to Dr H. C. Kao at NASA Lewis Research Centre for discussion about the topological arguments on the secondary flow, and also is indebted to Mr R. Cavicchi and to Dr David Jacqmin for careful reading of the manuscript and many kind comments.

REFERENCES

AGRAWAL, Y., TALBOT, L. & GONG, K. 1978 Laser anemometer study of flow development in curved circular pipes. *J. Fluid Mech.* **85**, 497.

BENJAMIN, T. B. 1978 Bifurcation phenomena in steady flows of a viscous fluid II. Experiments. *Proc. R. Soc. Lond.* A **359**, 27.

BRILEY, W. R. & MCDONALD, H. 1980 On the structure and use of linearized block implicit schemes. *J. Comp. Phys.* **34**, 54.

CHORIN, A. J. 1967 A numerical method for solving incompressible viscous flow problems. *J. Comp. Phys.* **2**, 12.

CLIFFE, K. A. & MULLIN, T. 1985 A numerical and experimental study of anomalous modes in the Taylor experiment. *J. Fluid Mech.* **153**, 243.

DEAN, W. R. 1927 Note on the motion of fluid in a curved pipe. *Phil. Mag.* **20**, 208.

DEAN, W. R. 1928 The stream-line motion of fluid in a curved pipe. *Phil. Mag.* **30**, 673.

DENNIS, S. C. R. & NG, M. 1982 Dual solution for steady laminar flow through a curved tube. *Q. J. Mech. Appl. Maths* **35**, 305.

EUSTICE, J. 1910 Flow of water in curved pipes. *Proc. R. Soc. Lond.* A **84**, 107.

EUSTICE, J. 1911 Experiments on stream-line motion in curved pipes. *Proc. R. Soc. Lond.* A **85**, 119.

HILLE, P., VEHRENKAMP, R. & SCHULZ-DUBOIS, E. O. 1985 The development and structure of primary and secondary flow in a curved square duct. *J. Fluid Mech.* **151**, 219.

HUMPHREY, J. A. C. 1977 Flow in ducts with curvature and roughness. Ph.D. thesis, Imperial College of Science and Technology.

HUMPHREY, J. A. C., CHANG, S. M. & MODAVI, A. 1982 Developing turbulent flow in a 180° bend and downstream tangent of square cross-section. *LBL Rep.* 14844. Berkeley.

HUMPHREY, J. A. C., TAYLOR, A. M. K. & WHITELAW, J. H. 1977 Laminar flow in a square duct of strong curvature. *J. Fluid Mech.* **83**, 509.

KAO, H. C., BURSTADT, P. L. & JOHNS, A. L. 1983 Flow visualization and interpretation of visualization data for deflected thrust V/STOL nozzle. *NASA TM*-83554.

MASLIYAH, J. H. 1980 On laminar flow in curved semicircular ducts. *J. Fluid Mech.* **99**, 469.

NANDAKUMAR, K. & MASLIYAH, J. H. 1982 Bifurcation in steady laminar flow through curved tubes. *J. Fluid Mech.* **119**, 475.

PATANKAR, S. V., PRATAP, V. S. & SPALDING, D. B. 1974 Prediction of laminar flow and heat transfer in helically coiled pipes. *J. Fluid Mech.* **62**, 539.

SOH, W. Y. 1987 Time-marching solution of incompressible Navier–Stokes equations for internal flow. *J. Comp. Phys.* **70**, 232.

SOH, W. Y. & BERGER, S. A. 1984 Laminar entrance flow in a curved pipe. *J. Fluid Mech.* **148**, 109.

SOH, W. Y. & BERGER, S. A. 1987 Fully developed flow in a curved pipe of arbitrary curvature ratio. *Intl J. Numer. Meth. in Fluids* **7**, 733.

WINTERS, K. H. 1984 A bifurcation study of laminar flow in a curved tube of rectangular cross-section. *AERE-TP*. 1104. AERE Harwell.